Nonlinear Predictive Energy Management of Residential Buildings with Photovoltaics & Batteries

Chao Sun, Fengchun Sun, and Scott J. Moura

Abstract—This paper studies a nonlinear predictive energy management strategy for a residential building with a rooftop photovoltaic (PV) system and second-life lithium-ion battery energy storage. A key novelty of this manuscript is closing the gap between building energy management formulations, advanced load forecasting techniques, and nonlinear battery/PV models. Additionally, we focus on the fundamental trade-off between lithium-ion battery aging and economic performance in energy management. The energy management problem is formulated as a model predictive controller (MPC). Simulation results demonstrate that the proposed control scheme achieves 96%-98% of the optimal performance given perfect forecasts over a long-term horizon. Moreover, the rate of battery capacity loss can be reduced by 25% with negligible losses in economic performance, through an appropriate cost function formulation.

I. Introduction

A. Background

Residential buildings equipped with photovoltaics and batteries (RBPB) have attracted significant interest for integrating distributed and renewable power generation into the smart grid [1]. The potential benefits include increased power flexibility, reduced emissions, and reduced operating costs. In these systems the photovoltaics (PVs) operate as a local electric generator, the batteries store energy, the building consumes electric energy, and the entire system interfaces with the electric grid. Economic viability and reliability depend critically on the energy management system, which governs power flow between generation, loads, and storage [2]. Optimized energy management is complicated by uncertain environmental conditions, load, and battery aging. In this paper, we develop a nonlinear predictive energy management scheme for a home with PV and second life battery energy storage, using data-based forecasting of environmental conditions, load, electricity prices, and grid emissions.

B. Relevant Literature

Energy management for RBPB applications is a rapidly growing research area. Rule-based energy management approaches have been widely studied, see e.g. [3], [4]. The

drawback of such schemes is that they lack a systematic design methodology and optimality. Consequently, model-based optimal energy management strategies are gaining interest [5], [6]. Linear programming (LP) and mixed-integer linear programming (MILP) are the most common formulations to compute optimal energy management control policies [7], [8], [9]. In reality, however, the photovoltaics and battery exhibit important nonlinear characteristics. For example, the mapping from solar irradiance and temperature to power output is nonlinear, motivating the maximum power point tracking problem [10]. Similarly, the mapping from battery state-of-charge and current to output voltage is nonlinear. Interestingly, nonlinear energy management for RBPB systems has not been well studied. The model predictive control (MPC) framework is ideally suited for RBPB energy management [11], since it incorporates potentially nonlinear mathematical models and explicitly enforces constraints.

Uncertain PV power generation and building load is a second critical challenge. PV power can be predicted by combining internet-based forecasts of environmental conditions (e.g. solar irradiation and air temperature) with photovoltaic models [12]. Building load forecasting is an extremely rich topic within itself (c.f. review article [13]). However, the relationship between forecasting error and energy management performance is less well understood. Most previous studies on RBPB energy management assume loads are known *a priori*, e.g. [9], [14], [15], [16], or consider average load models with Gaussian noise, e.g. [7], [8]. This provides an opportunity to close the gap between advancements in the building load forecasting literature and RBPB energy management.

A third challenge is battery life. That is, one expects that leveraging battery energy storage enhances economic performance metrics, at the sacrifice of long-term battery cycle life. The nature of this trade off is not well-understood. References [14], [15] have considered battery aging using a simple linear capacity fade model for lead-acid batteries. To the best of the authors' knowledge, no existing studies have considered aging for the lithium-ion chemistry in RBPB systems.

C. Contributions

This article's main contribution is a comprehensive framework for predictive home energy management that includes local generation, storage, and demand. Specific novelties within this framework include:

- Nonlinear MPC formulation of the energy management problem for RBPB systems, with a Liu-Jordan solar irradiation model, equivalent circuit PV and battery models,

and a Li-ion cycle-life battery degradation model.

- Introducing load forecasting into the RBPB energy management via artificial neural networks (ANNs), motivated by [13]. We specifically study economic performance loss as a function of increasing load forecast error.
- Incorporating an empirical lithium-ion battery capacity loss model into the optimization formulation. This enables us to study the fundamental tradeoffs between cost and battery aging in the energy management design [17].

The remainder of the paper is organized as follows. In Section II, the RBPB configuration and system model is presented. Section III develops and validates a data-driven load forecast model. Section IV details the model predictive controller. Simulation results and sensitivity studies are illustrated in Section V, followed by key conclusions in Section VI.

II. RESIDENTIAL BUILDING-PV-BATTERY SYSTEM

In Fig. 1(a) the RBPB is composed of a PV array, a second-life[1] lithium-ion battery pack, the building's electrical loads, the utility grid, various power converters, real-time Internet-based data feeds, and the energy management algorithm. The battery reconciles imbalance between available PV power and load. The power flow topology is detailed in Fig. 1(b). The PV and battery are coupled to a DC bus connected to a DC/AC inverter to power AC loads and interact with the grid. Note that we assume energy cannot be exported to the grid, although it is trivial to extend this framework to allow energy exports. Other generators, such as wind turbines or fuel cells, can also be integrated into the network with appropriate models.

The controller's role is to manage power flow between these components to optimize objectives such as electricity cost, grid power plant emissions, or battery health, subject to safe operating constraints. Specifically, a predictive scheme is applied that leverages real-time Internet-based data to forecast home load and PV power. Next we detail sub-models for the RBPB components.

A. Mathematical Subsystem Models

1) Solar Irradiation: A Liu-Jordan model is adopted to determine the solar flux and PV panel temperature [18]. The solar irradiation includes the global horizontal irradiance S_{gh}, the direct beam irradiance S_{db}, and the diffuse irradiance S_{di}. The effective solar irradiance is given by

$$S_{pv} = S_{db}(\cos\theta_s \cos\beta_p + \sin\theta_s \sin\beta_p \cos(\alpha_s - \alpha_p)) \\ + S_{di}(1 + \cos\beta_p)/2 + S_{gh}\rho_g(1 - \cos\beta_p)/2, \quad (1)$$

where θ_s, α_s are the zenith angle and azimuth angle of the sun, respectively; α_p, β_p are the azimuth angle and altitude tilt angle of the PV panel, respectively; ρ_g is the diffuse reflectance rate of the ground. The panel temperature is

$$T_{pv} = S_{pv}e^{(a+bv_w)} + T_a, \quad (2)$$

[1] "Second-life" means the battery pack is reused from an automotive application, such as a hybrid electric vehicle.
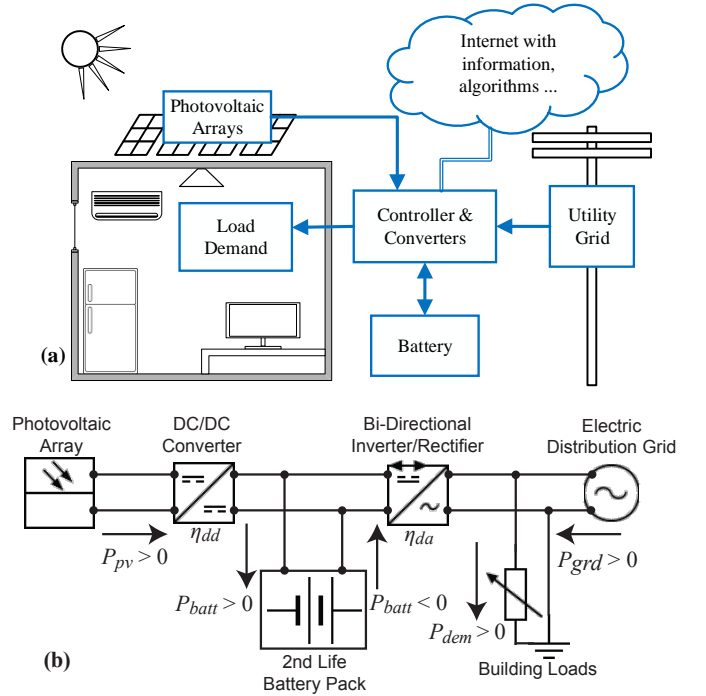

Fig. 1. The residential building with photovoltaics and battery energy storage: (a) the system configuration; (b) the power flow and topology.

where T_a, v_w are ambient temperature and wind speed, and a, b are empirical parameters. In the case studies examined here, all climatological data is collected from [19].

2) Photovoltaic Array: The PV cell is modeled as an equivalent circuit [20]. This model consists of an ideal current source I_{cs} in parallel with a diode and resistance R_p all in series with resistor R_s. The diode models the semiconductor material, and R_s models the resistance between the contactor and semiconductor material. The governing equations are

$$V_d = V_{cell} + I_{pv}R_s, \quad (3)$$

$$I_{pv} = I_{cs} - I_s\left[e^{\left(\frac{qV_d}{AkT_{pv}}\right)} - 1\right] - \frac{V_d}{R_p}, \quad (4)$$

$$I_s = I_{s,r}\left(\frac{T_{pv}}{T_r}\right)^3 e^{\frac{qE_{bg}}{Ak}\left(\frac{1}{T_r} - \frac{1}{T_{pv}}\right)}, \quad (5)$$

$$I_{cs} = [I_{cs,r} + K_I(T_{pv} - T_r)]\frac{S_{pv}}{1000}, \quad (6)$$

where V_d and V_{cell} are the diode voltage and PV cell voltage, respectively; I_{pv} is the PV cell output current, and I_s is the cell saturation current; q, A and k are an electron charge, an ideal factor, and the Boltzmann's constant, respectively; $I_{s,r}$ is the cell's reverse saturation current at reference temperature T_r; E_{bg} is the band-gap energy of the semiconductor; $I_{cs,r}$ is the reference short-circuit current of the PV cell at 25°C and 1kW/m². K_I is the cell's short-circuit current temperature coefficient. The cell model is scaled to an PV array by considering n_{pv} cells in series [10], thus the array power is

$$P_{pv} = n_{pv}V_{cell}I_{pv}. \quad (7)$$

For brevity, we only summarize the PV model equations

here from (3) to (7). Further details can be found in [10]. Note that a maximum power point tracking (MPPT) algorithm is usually employed to improve PV efficiency.

3) Second-life Battery: Second-life batteries are included in the RBPB. The battery pack is modeled as an equivalent circuit [21]. The electrical power at the battery terminals is denoted by P_{batt}, and the battery state-of-charge is denoted by SOC. The governing equations are,

$$P_{batt}(t) = V_{oc}I_{batt}(t) - I_{batt}^2(t)R_{in}, \qquad (8)$$

$$\dot{\text{SOC}}(t) = -\frac{I_{batt}(t)}{Q}, \qquad (9)$$

where I_{batt} is the battery current; V_{oc}, R_{in} and Q are the open circuit voltage, the internal resistance and the battery capacity, respectively. $P_{batt} > 0$ corresponds to discharging, whereas $P_{batt} < 0$ corresponds to charging. In practice, the model parameters need to be characterized through experiments, and additional efforts are required to eliminate inconsistencies between different cells [22].

A cycle-life model developed in [23] for LiFePO$_4$-C cells is considered to account for Li-ion battery degradation. Denote the percentage of battery capacity loss by Q_{loss}. The capacity loss model is given by

$$Q_{loss} = B_{exp}e^{\left(\frac{-31700+370.3\times C_{rate}}{RT_{batt}}\right)}(A_h)^{0.55}, \qquad (10)$$

where B_{exp} is the pre-exponential factor, which decreases with increasing C-rate; R is the gas constant; T_{batt} is the absolute temperature of the battery; A_h is the processed energy capacity in Ah. We shall use this model to explore the trade off between cost minimization and battery aging. Indeed, other degradation models can be considered as well (see models within [17]).

4) Conservation of Power: The home power demand P_{dem} and grid utility power P_{grd} satisfy the power conservation law,

$$P_{dem}(t) = P_{grd}(t) + \eta_{dd}\eta_{da}P_{pv}(t) + \eta_{da}^{\text{sign}(P_{batt})}P_{batt}(t), \quad (11)$$

where η_{dd} is the efficiency of the DC/DC converter; η_{da} is the efficiency of the DC/AC inverter. In this case study, we assume constant values for η_{dd}, η_{da}, but these can be power-dependent with appropriate model extensions.

Equations (1)-(11) summarize the subsystem models used for the MPC (see Section IV). Next we study a data-driven load forecasting algorithm.

III. DATA ENABLED LOAD FORECASTING

A. Load Data Analysis

We analyze load data from a single family home in Los Angeles to investigate correlations between load and season, temperature, day of week, and time of day. The objective is to determine inputs for a data-driven load forecast model. The collected data corresponds to date range 2013-04-01 to 2014-03-31. Figure 2 plots the hourly, daily, monthly and yearly average electricity consumption. The hourly load varies between 0.5 kW to 4 kW. The yearly average load is about 1 kW. This house consumed more energy in August-September (hottest months), and December-January (coldest months) relative to
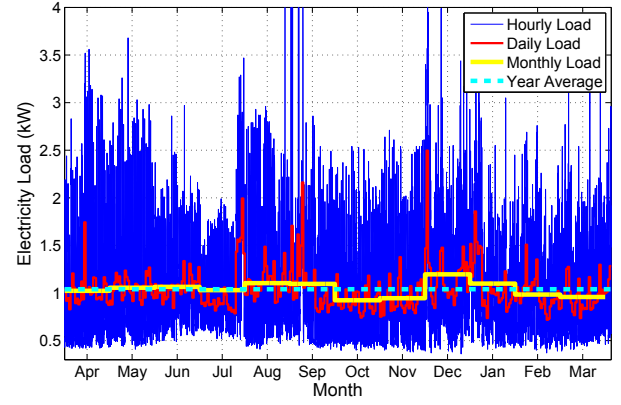

Fig. 2. Electricity consumption of a single family home in Los Angeles from 2013-04-01 to 2014-03-31.
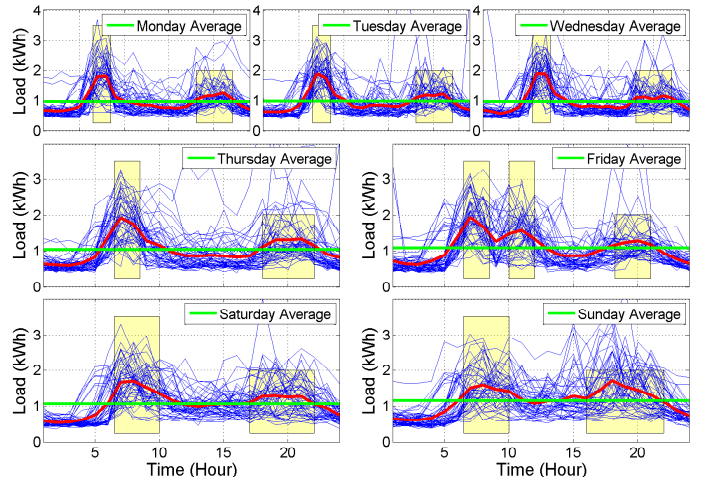

Fig. 3. Electric load from Monday to Sunday of the sampled LA data. Blue: load of particular week days; red: hourly average load across all weeks; green: daily average load over all weeks; yellow rectangle: peak load periods.

the other months. The correlation between the weekly average load and the weekly average temperature of this geographical area is also investigated. The results indicate that more energy is consumed when the weekly average temperature is higher than 21°C or lower than 14°C. That is, the relationship between weekly average temperature and load is nonlinear.

In Fig. 3, the load data is classified according to the day of week. From Monday to Thursday, the daily pattern of electricity consumption is similar. Peak loads consistently occur from 7:00 to 8:30 AM, and 6:00 to 10:00 PM. On Fridays, the pattern changes. There are two peak loads observed in the morning, which is clearly different from the Monday-Thursday pattern. During weekends, the electricity consumption pattern exhibits higher variance. The peak loads on Saturday and Sunday are generally broader. The daytime off-peak load is also higher compared with the weekdays.

From this analysis, we determined temperature, day-of-week, and time-of-day to be appropriate exogenous inputs for the data-driven model (see Section III-B). Other information, such as holidays and personal habits, could potentially be in-
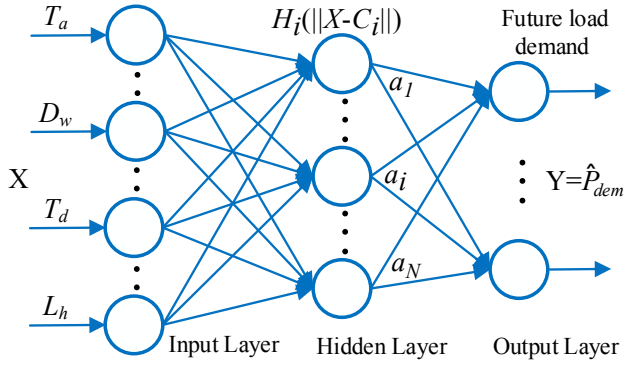
Fig. 4. Artificial Neural Network (ANN) model structure for forecasting residential building electric loads. Symbols T_a, D_w, T_d, L_h are the ambient temperature, day-of-week, time-of-day, and historical loads, respectively.
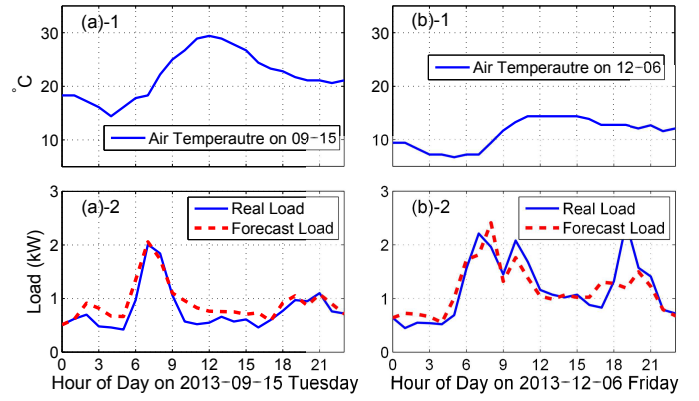

Fig. 5. Forecast examples and corresponding air temperature for the LA load data: (a) 2013-09-15 Tuesday; (b) 2013-12-06 Friday. The prediction length is 24-hour in these examples.

corporated into the forecast model. However, we demonstrate in Section V-A that a simple load forecasting method achieves 96%-98% performance relative to perfect forecasts.

B. Load Demand Forecast

We consider a radial basis function neural network (RBF-NN) forecast algorithm to forecast short-term loads. RBF-NN is selected because it captures the nonlinear input-output relations of home load and achieves reasonable forecast accuracy. Other forecasting methods may be considered as well [13]. Generally, the RBF-NN model contains three layers: the input layer, the hidden layer, and the output layer, shown in Fig. 4. The hidden layer performs nonlinear transforms for feature extraction, and the output layer is a linear combination of the basis functions. The Gaussian function is used as the radial basis function in the hidden layer [13]. Mathematically,

$$Y = f_{ANN}(X) = \sum_{i=1}^{N} a_i \cdot H_i \left(\|X - C_i\| \right) \quad (12)$$

$$H_i \left(\|X - C_i\| \right) = \exp \left[-\frac{1}{2\sigma_i^2} \|X - C_i\|^2 \right] \quad (13)$$

where a_i is the neuron weight, C_i is the basis function center, and σ_i is the spread width. Parameters a_i, C_i, σ_i for $i = 1, \cdots, N$ are fit on training data using the Levenberg-Marquardt algorithm.

Based on the data analysis in Section III-A, the air temperature, day of week, and time of day are selected as exogenous inputs to the RBF-NN model. Short-term historical load is an endogenous input. Thus, the input vector X is defined as

$$X = [\hat{T}_a \ D_w \ T_d \ L_h], \quad Y = \left[\hat{P}_{dem,k+1}, \cdots, \hat{P}_{dem,k+m} \right] \quad (14)$$

where $\hat{T}_a$ is the forecasted air temperature obtained via Internet-based weather services. Symbol T_a is the true air temperature and used only during training; D_w is the day of week; T_d is the time of day; L_h is the historical load. The output of the forecast algorithm Y is the future $m-$dimensional load vector, denoted as $\hat{P}_{dem}$. The model is trained and validated on collected load data, as described next.

C. Load Demand Forecast Validation

The RBF-NN forecast model is validated in this subsection. The validation data is one-year of measured electricity consumption data (2013-04-01 to 2014-03-31) collected from two houses located in Los Angeles (LA) and Berkeley, California USA. The first half year is used for neural network training, and the second half year is used for cross validation. The sampling period is one hour. The length of the historical load (in the input vector) and the length of the prediction horizon (output vector) are both set as 24 hours.

Fig. 5(a) and (b) demonstrate two forecast examples in the LA data test on 2013-09-15 Tuesday and 2013-12-06 Friday, respectively. The former corresponds to a warm autumn day, and the latter corresponds to a chilly winter day. Fig. 5(a) exemplifies the RNF-NN's ability to forecast a typical weekday. The characteristic morning and evening peaks are both predicted. In Fig. 5(b), the lowest air temperature is 5°C, resulting a relatively high loads due to heating. The two-morning-peaks on Friday are also predicted.

An empirical cumulative distribution function (CDF) of all the root mean square errors (RMSEs) are demonstrated in Fig. 6(a). Note that 80% of the RMSEs are below 0.45 kW and 0.55 kW in the LA and Berkeley data, respectively. Indeed, higher accuracy forecasting algorithms exist [13]. However, we show that this RBF-NN model is sufficiently accurate for predictive energy management - a claim that is quantified and verified in Section V-A.

Sensitivity to the input historical load length is also investigated. The average RMSE of the LA and Berkeley data with different historical load lengths is illustrated in Fig. 6(b). As expected, longer historical load vectors produce increased forecast accuracy. Interestingly, the marginal accuracy improvement decreases dramatically for historical load vectors greater than six hours. Conversely, the most recent five hours of load significantly impact forecasting accuracy.

D. Weather, Cost, and Emission Forecasts

Internet-based meteorological forecast services are now ubiquitous. Namely, solar irradiance and air temperature data
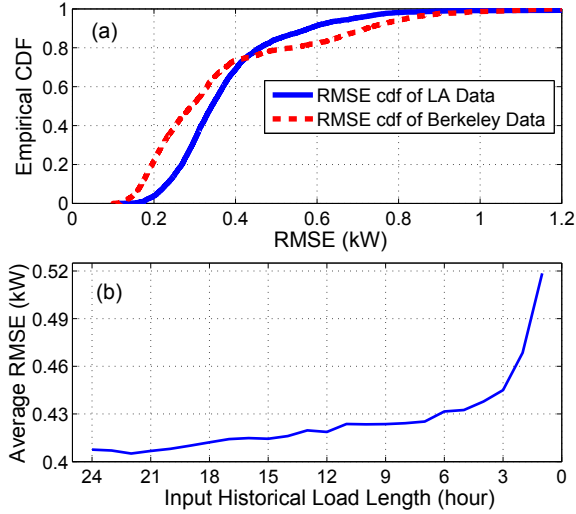
Fig. 6. (a): Empirical CDF for forecast RMSE of the LA and Berkeley load data; (b): Average RMSEs of the LA and Berkeley data with different historical load lengths used in the RBF-NN input (output is 24-hour long).

streams are easily accessible via application programming interfaces (APIs). The acquired irradiation and temperature information is injected into the solar irradiation model (see Section II-A1) to estimate the PV solar flux and PV temperature, denoted as $\hat{S}_{pv}$ and $\hat{T}_{pv}$, respectively.

In addition, the electric cost and power plant carbon emissions are incorporated into the objective function (see Section IV). This information is also assumed to be available from the Internet[2]. The observed electric rate and unit carbon emission are notated as R_e and C_e, respectively.

IV. MODEL PREDICTIVE CONTROL

The proposed predictive energy management strategy determines the optimal power flow, given real-time forecasted load, weather conditions, and electricity cost obtained from the Internet. Given the system model (1)-(11), we require one control input to render a casual system, and select grid power $u(t) = P_{grd}(t)$. Denoting $x(t)$ as the state variable, $u(t)$ as the control variable, $d(t)$ as the system disturbance, and $y(t)$ as the output, the system model is

$$\dot{x}(t) = f(x(t), u(t), d(t)), \quad y(t) = g(x(t), u(t), d(t)), \quad (15)$$

with $x(t) = \text{SOC}(t)$, $u(t) = P_{grd}(t)$, $y(t) = P_{batt}(t)$. The disturbance $d(t) = [\hat{P}_{dem}(t), \hat{S}_{pv}(t), \hat{T}_{pv}(t)]^T$, where $\hat{P}_{dem}(t)$, $\hat{S}_{pv}(t)$, and $\hat{T}_{pv}(t)$ are the forecasted load, solar irradiation and PV temperature, respectively. The electricity cost and carbon emission can be calculated by

$$E_r(u,t) = R_e(t) \cdot u(t), \quad E_c(u,t) = C_e(t) \cdot u(t), \quad (16)$$

where $R_e(t)$ and $C_e(t)$ are time-varying electric rate and unit carbon emission, respectively. The objective function is

$$E(u,t) = \lambda_1 \cdot \frac{E_r(u,t)}{E_{r,\max}} + \lambda_2 \cdot \frac{E_c(u,t)}{E_{c,\max}}, \quad (17)$$

where $\lambda_1, \lambda_2 \in [0,1]$ are weighting parameters and $E_{r,\max} = \max_u \max_t E_r(u,t), E_{c,\max} = \max_u \max_t E_c(u,t)$. For simplicity, we fix the prediction horizon length equal to the control horizon, namely L_p. Assume the time step is Δt. At time $k\Delta t$, the cost function J_k is formulated as

$$J_k = \int_{k\Delta t}^{(k+L_p)\Delta t} E(u,t)^2 \, dt. \quad (18)$$

Additionally, the following inequality constraints must hold:

$$\text{SOC}^{\min} \leq \text{SOC} \leq \text{SOC}^{\max}, \ I_{batt}^{\min} \leq I_{batt} \leq I_{batt}^{\max}, \\ P_{batt}^{\min} \leq P_{batt} \leq P_{batt}^{\max}, \ P_{grd}^{\min} \leq P_{grd} \leq P_{grd}^{\max}. \quad (19)$$

Note that inequality constraint $P_{grd} \leq P_{grd}^{\max}$ enforces peak shaving and regulates any peak load magnitude charges. Special consideration is also given to the battery terminal SOC constraint during each receding horizon of the MPC to restrict battery charge depletion. That is, the terminal SOC must be within a small neighborhood of the reference value,

$$\left(\text{SOC}((k+L_p)\Delta t) - \text{SOC}^{\text{ref}}\right)^2 \leq \varepsilon, \quad (20)$$

where SOC^{ref} is a pre-defined constant. Consequently, the MPC algorithm steps are:

1) Acquire the forecasted load, weather conditions, electric rate and unit carbon emission from the Internet;
2) Compute optimal control policy via MPC;
3) Apply the first time-step of the optimal control policy to the RBPB;
4) Measure the system states, update system constraints, and repeat the procedure at the next time step.

Due to the nonlinearities in the PV model (3)-(7) and battery model (8)-(9), dynamic programming (DP) is employed in step two to solve the constrained nonlinear optimization problem at each time step [24]. Alternative nonlinear formulations that admit special structure, e.g. linear or convex programs, can utilize corresponding solvers [7], [8], [9]. DP is used here for its generality and provable optimality.

V. SIMULATION AND ANALYSIS

A. Energy Management for Economics & Emissions

Parameters for the case study RBPB are listed in Table I. The battery pack parameters are adopted from a Toyota Prius hybrid electric vehicle, and we assume the second-life pack has already degraded to 80% of its original energy capacity. We consider 6 PV panels in series per pack and 5 packs in parallel. The energy management control time step is selected as 1 hour. In practice, faster dynamics are governed by lower level controllers.
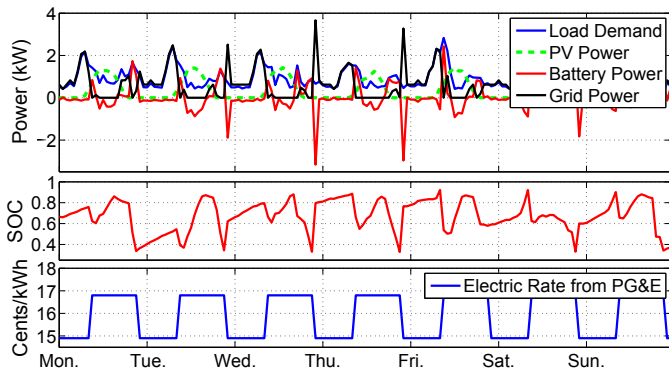
Fig. 7. Week-long power, SOC, and electric rate trajectories of the proposed predictive energy management scheme on the LA home, for $\lambda_1 = 1, \lambda_2 = 0$ in cost function (17), with 24-hr ahead RBF-NN load forecasting.
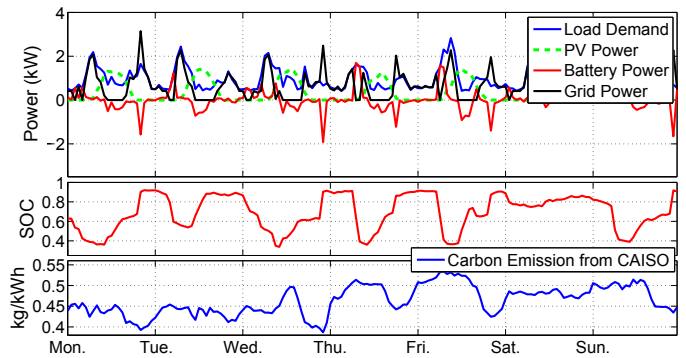

Fig. 8. Week-long power, SOC, and carbon emission trajectories of the proposed predictive energy management scheme on the LA house when $\lambda_1 = 0, \lambda_2 = 1$ in cost function (17), with 24-hr ahead RBF-NN load forecasting.

TABLE I
GENERAL PARAMETERS OF THE RBPB SYSTEM

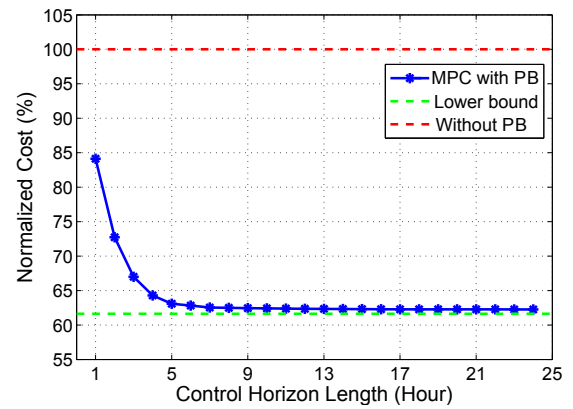|		
	Cell Type	Monocrystalline
PV Panel	Cell Area	156×156 mm
(Renogy Monocrystalline 250D)	Cell Number	60 per panel
	Max Power	250 W
Battery Pack	Cell Chemistry	C-LiFePO$_4$
(Nominal)	Energy Capacity	1.3 kWh for pack
	Charge Capacity	6.5 Ah per Cell
	Cell Number	168

Fig. 9. Normalized performance when increasing the MPC control horizon length from 1hr to 24hr. The proposed strategy is represented as (MPC with PB, in solid blue). The cost without PV/battery is normalized to 100% (Without PB, in dashed red). (Lower bound, in dashed green) is the best-case solution with a one-week time horizon and perfect forecasts.

1) Cost versus Carbon: The control and prediction horizon is 24 hours. The electricity load data is collected data from single family homes in LA and Berkeley. The demand during each control horizon is predicted by the RBF-NN forecast model. The temperature, irradiance, electricity price and carbon emission data are obtained from the National Climatic Data Center [19], PG&E and WattTime.org, respectively. The controller accesses this data in real-time via APIs.

First, we consider $\lambda_1 = 1, \lambda_2 = 0$ in the cost function (17) to investigate the optimal behavior with respect to electric cost only. A week-long energy management result is shown in Fig. 7. The PV power follows a diurnal cycle. During the day, the solar energy is directly used to power the house. Surplus energy is stored in the battery for future use. When solar energy is insufficient to satisfy load, the battery or grid provides support. The bottom figure shows a two-tiered cost structure, including higher-cost "on-peak" rates and lower-cost "off-peak" rates. To reduce the electricity cost, the controller avoids on-peak grid power as much as possible, as demonstrated in Fig. 7. Consequently the battery generally charges during off-peak periods, and discharges during on-peak periods.

A similar simulation result is shown in Fig. 8, where the objective is to minimize carbon emissions E_c only, i.e. $\lambda_1 = 0$, $\lambda_2 = 1$. One can visually observe the grid power trajectory is anti-correlated with marginal carbon emissions.

2) Horizon Length Determination: Next we examine control horizon length. Figure 9 depicts the MPC performance (MPC with PB, in solid blue) for control horizons ranging

from 1 hr. to 24 hrs. The cost is normalized to the electric cost without a PV and battery (Without PB, in dashed red). For a 1 hr. horizon, the MPC is short-sighted and normalized cost is about 85%. As the control length increases, the performance converges toward the lower bound (green dashed). This lower bound differs from MPC in two ways: (i) the load forecasts are perfect and (ii) the optimization is performed over one week without a rolling horizon. When the control length is 7 hours, the cost is 2% greater than the lower bound (approximately 64%). Consequently, one can reach within 2% of the lower cost bound with a 7 hr. control horizon and imperfect meteorological/load forecasts. Improvements are negligible with increased control horizons beyond 7 hrs.

3) Performance Assessment: Ten weeks are randomly selected from the LA and Berkeley data sets for a comprehensive assessment of the controller. Summarized results are listed in Table II. The cost and carbon (subscripts '$' and 'cb' respectively) are reported by symbols C, P and σ in respective quantities of USD/kg, percentage, and the standard deviation. We can see that both the electricity cost and carbon emission can be reduced by over 35% compared to homes

Type	$C_\$$	$P_\$$	$\sigma_\$$	C_{cb}	P_{cb}	σ_{cb}
Without PB	27.32	100%	–	8.03	100%	–
MPC with PB	17.54	64.2%	+/-0.8%	5.07	63.1%	+/-1.2%
Lower Bound	16.97	62.1%	+/-0.3%	4.93	61.4%	+/-0.7%

(rt indicated for the electric rate, and cb means the carbon emission.)

without PV/battery. Moreover, the nonlinear predictive energy management is only 2% worse than the lower bound. This suggests moderately accurate forecasts of load are sufficient for near-optimal cost/carbon reductions.

4) Forecast Error Sensitivity Study: Next we investigate how demand forecasting error impacts energy management performance. To conduct this sensitivity study, we append additive uniformly distributed random errors to the real load data. The RMSE of the contaminated demand forecast is increased from 0 to 1 (kW) in Fig. 10.

Over 200 tests with uniformly distributed errors are conducted, along with 20 tests with our proposed RBF-NN forecasting model, shown in Fig. 10. When the RMSE is below 0.3 kW, the controller performs near the lower bound, with normalized costs between 62% and 64% relative to the no PV/battery scenario. As forecast RMSE increases, the normalized cost increases linearly. Note that the average load for the LA home is 1 kW. Consequently, an RMSE of 0.5 kW represents a 50% normalized RMSE. Nevertheless, the MPC scheme is only 4% worse than the lower bound.

Additionally, we note the RMSE of the RBF-NN forecaster is near 0.38 kW. The normalized cost is 63.4%, which equals the performance of contaminated forecasts with 0.25 kW RMSE. This result is unexpectedly good – only 1.5-2% higher than the lower bound. After comparison, we found the RMSE produced by the RBF-NN has a tighter distribution (i.e. smaller variance) compared to uniformly distributed errors. This indicates the RBF-NN forecast model captures the nonlinear load data characteristics and provides useful predictions for MPC, relative to the performance achieved with perfect forecasts.

B. Battery Health Conscious Control

In this part, we incorporate a battery capacity loss model into the objective function (18), as described in Section II-A3. The MPC cost function is reformulated from (18) as

$$J_k = \int_{k\Delta t}^{(k+L_p)\Delta t} \left(\lambda E_r^2(u,t) + (1-\lambda)Q_{loss}^2(u) \right) dt, \quad (21)$$

where λ is a weighting parameter, E_r and Q_{loss} are normalized into the same scale.

A comparison of the controller behavior on the November 2013 LA data with different λ values is shown in Fig. 11. Figure 11(a) shows the battery cell C-rate[3] distribution over SOC. When $\lambda = 1$, the cost function emphasizes electric cost only and the C-rate spreads to as high as 0.5C for charging, and as low as -0.5C for discharging. Charging C-rates greater

[3]C-rate is a normalized measure of current, useful for comparing batteries of different sizes. C-rate = $I(t)/Q$.
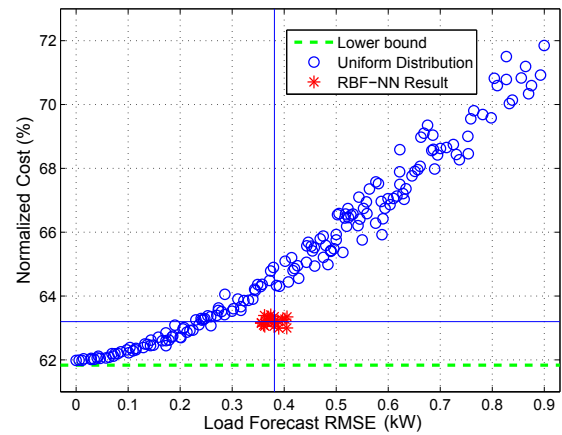

Fig. 10. Normalized energy management performance of the artificially formulated load with uniformly distributed RMSEs from 0 to 1, compared with the RBF-NN energy management results.
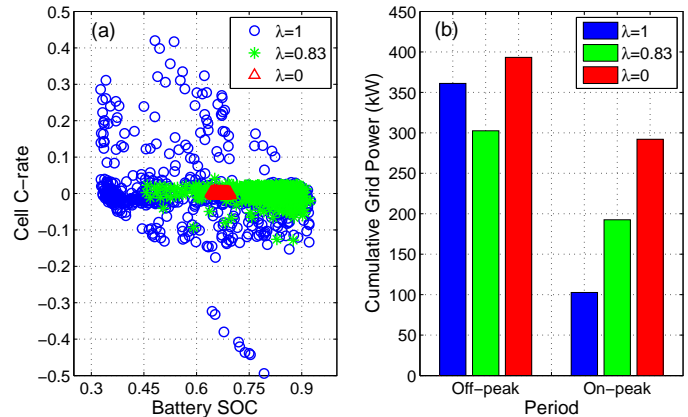

Fig. 11. Cell C-rate and grid power usage comparison for November 2013 LA data, when $\lambda \in \{1, 0.83, 0\}$ in cost function (21).

than 0.1C occur more frequently when SOC < 0.65. When $\lambda = 0.83$, the solution reserves some battery power to mitigate battery aging. The maximum charge and discharge C-rates are restricted within 0.1C and -0.2C, respectively. When $\lambda = 0$, the cost function emphasizes battery health only. In this case, C-rate is limited between 0.02C and -0.02C and the battery SOC changes negligibly. Consequently, the battery is effectively unused to avoid degradation.

The corresponding cumulative grid power is visualized in Fig. 11(b). As elaborated above, when $\lambda = 0$ the battery is inactive. Therefore, more power is required from both the off-peak and on-peak periods to satisfy load. On the contrary, when λ increases, the battery stores excess PV power and reduces grid power. As λ continues to increase, the controller becomes more aggressive about exploiting price arbitrage. This 'buffering' behavior is evident from the grid power comparison between $\lambda = 1$ and 0.83 in Fig. 11(b). It is notable that cumulative on-peak power is reduced by nearly 50% between $\lambda = 0.83$ and 1. This reduction is partially compensated by a 17% increase in off-peak power for $\lambda = 1$.

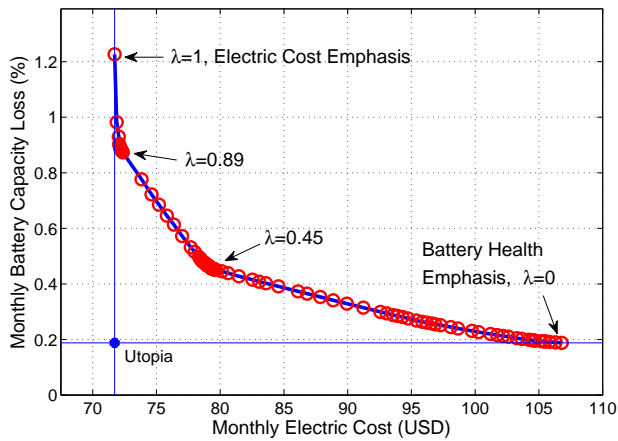Six arbitrarily selected months from the LA data and

Fig. 12. Average electric cost and battery degradation for one month, with different λ inserted into cost function (21).

Berkeley data set are used for the battery health conscious control study, by varying λ from 1 to 0 in 0.01 increments. Costs and capacity loss per month are illustrated in Fig. 12. When $\lambda = 1$, the controller minimizes electric cost only, and battery capacity degrades by 1.2% per month. The absolute minimum electricity cost is 72 USD/month. As λ decreases to 0.89, the battery capacity loss is reduced from 1.2% to 0.9% with nearly negligible increase in electric cost. When λ is less than 0.89, the battery degradation continues decreasing, but with smaller gradient. The rate-payer must pay 2 USD/month for reducing monthly battery capacity loss by 0.1% when the λ exists between 0.89 and 0.45. For $\lambda < 0.45$, the battery degradation can hardly be attenuated further. The user would pay over 11 USD/month to save 0.1% battery capacity, which is 5 times higher than before the $\lambda = 0.45$ point. The minimal battery capacity loss is 0.2% per month when $\lambda = 0$. The electric cost reaches a maximum of 107 USD/month – 49% higher than the minimum.

VI. CONCLUSIONS

This paper presents a nonlinear data-enabled predictive energy management strategy for a residential building with photovoltaics (PV) and battery energy storage. A model predictive controller (MPC) is formulated with nonlinear PV and battery models, and a RBF-NN load forecasting algorithm. Future weather conditions are acquired from meteorological data steams and integrated into the MPC formulation. Numerical experiments demonstrate the proposed predictive energy management system achieves 96%-98% optimality of the perfect forecast lower bound, with respect to electric cost and carbon emissions. In addition, we study the trade off between battery aging and cost minimization. The controller's sensitivity to control horizon length, load forecast accuracy, and battery health are investigated to explore the fundamental tradeoffs.

REFERENCES

[1] N. Hatziargyriou, H. Asano, R. Iravani, and C. Marnay, "Microgrids," *IEEE Power and Energy Magazine*, vol. 5, no. 4, pp. 78–94, 2007.

[2] D. E. Olivares, A. Mehrizi-Sani, A. H. Etemadi, C. Canizares, R. Iravani, M. Kazerani, A. H. Hajimiragha, O. Gomis-Bellmunt, M. Saeedifard, R. Palma-Behnke, *et al.*, "Trends in microgrid control," *IEEE Transactions on Smart Grid*, vol. 5, no. 4, pp. 1905–1919, 2014.

[3] H. Kanchev, D. Lu, F. Colas, V. Lazarov, and B. Francois, "Energy management and operational planning of a microgrid with a pv-based active generator for smart grid applications," *IEEE Transactions on Industrial Electronics*, vol. 58, no. 10, pp. 4583–4592, Oct 2011.

[4] M. Sechilariu, B. Wang, and F. Locment, "Building integrated photovoltaic system with energy storage and smart grid communication," *IEEE Transactions on Industrial Electronics*, vol. 60, no. 4, pp. 1607–1618, 2013.

[5] H. Karami, M. Sanjari, S. Hosseinian, and G. Gharehpetian, "An optimal dispatch algorithm for managing residential distributed energy resources," *IEEE Transactions on Smart Grid*, vol. 5, no. 5, pp. 2360–2367, Sept 2014.

[6] B. Jiang and Y. Fei, "Smart home in smart microgrid: A cost-effective energy ecosystem with intelligent hierarchical agents," *IEEE Transactions on Smart Grid*, vol. PP, no. 99, pp. 1–1, 2014.

[7] A. Nottrott, J. Kleissl, and B. Washom, "Energy dispatch schedule optimization and cost benefit analysis for grid-connected, photovoltaic-battery storage systems," *Renewable Energy*, vol. 55, pp. 230 – 240, 2013.

[8] X. Guan, Z. Xu, and Q.-S. Jia, "Energy-efficient buildings facilitated by microgrid," *IEEE Transactions on Smart Grid*, vol. 1, no. 3, pp. 243–252, Dec 2010.

[9] C. Clastres, T. H. Pham, F. Wurtz, and S. Bacha, "Ancillary services and optimal household energy management with photovoltaic production," *Energy*, vol. 35, no. 1, pp. 55–64, 2010.

[10] S. J. Moura and Y. A. Chang, "Lyapunov-based switched extremum seeking for photovoltaic power maximization," *Control Engineering Practice*, vol. 21, no. 7, pp. 971–980, 2013.

[11] G. Bruni, S. Cordiner, V. Mulone, V. Rocco, and F. Spagnolo, "A study on the energy management in domestic micro-grids based on model predictive control strategies," *Energy Conversion and Management*, 2015.

[12] E. Perez, H. Beltran, N. Aparicio, and P. Rodriguez, "Predictive power control for PV plants with energy storage," *IEEE Transactions on Sustainable Energy*, vol. 4, no. 2, pp. 482–490, 2013.

[13] H. S. Hippert, C. E. Pedreira, and R. C. Souza, "Neural networks for short-term load forecasting: A review and evaluation," *IEEE Transactions on Power Systems*, vol. 16, no. 1, pp. 44–55, 2001.

[14] Y. Riffonneau, S. Bacha, F. Barruel, and S. Ploix, "Optimal power flow management for grid connected pv systems with batteries," *IEEE Transactions on Sustainable Energy*, vol. 2, no. 3, pp. 309–320, 2011.

[15] Y. Ru, J. Kleissl, and S. Martinez, "Storage size determination for grid-connected photovoltaic systems," *IEEE Transactions on Sustainable Energy*, vol. 4, no. 1, pp. 68–81, 2013.

[16] C. Chen, S. Duan, T. Cai, B. Liu, and G. Hu, "Smart energy management system for optimal microgrid economic operation," *IET Renewable Power Generation*, vol. 5, no. 3, pp. 258–267, May 2011.

[17] S. Moura, J. Stein, and H. Fathy, "Battery-Health Conscious Power Management in Plug-In Hybrid Electric Vehicles via Electrochemical Modeling and Stochastic Control," *IEEE Transactions on Control Systems Technology*, vol. 21, no. 3, pp. 679–694, 2013.

[18] B. Liu and R. Jordan, "Daily insolation on surfaces tilted towards equator," *ASHRAE J. (United States)*, vol. 10, 1961.

[19] U.S. Local Climatological Data. NOAA/NCEI. Boulder, Colorado, USA. [Online]. Available: https://www.ncdc.noaa.gov/cdo-web/

[20] G. Vachtsevanos and K. Kalaitzakis, "A hybrid photovoltaic simulator for utility interactive studies," *IEEE Transactions on Energy Conversion*, no. 2, pp. 227–231, 1987.

[21] X. Hu, S. Li, and H. Peng, "A comparative study of equivalent circuit models for Li-ion batteries," *Journal of Power Sources*, vol. 198, pp. 359–367, 2012.

[22] S. J. Tong, A. Same, M. A. Kootstra, and J. W. Park, "Off-grid photovoltaic vehicle charge using second life lithium batteries: An experimental and numerical investigation," *Applied Energy*, vol. 104, pp. 740–750, 2013.

[23] J. Wang, P. Liu, J. Hicks-Garner, *et al.*, "Cycle-life model for graphite-LiFePO$_4$ cells," *Journal of Power Sources*, vol. 196, no. 8, pp. 3942–3948, 2011.

[24] E. V. Denardo, *Dynamic programming: models and applications*. Courier Dover Publications, 2003.